Anal Bioanal Chem (2007) 387:1705–1715
DOI 10.1007/s00216-006-0879-2

ORIGINAL PAPER

A new sample substrate for imaging and correlating organic and trace metal composition in biological cells and tissues

Lisa M. Miller · Qi Wang · Randy J. Smith · Hui Zhong · Donald Elliott · John Warren

Received: 14 August 2006 / Revised: 19 September 2006 / Accepted: 21 September 2006 / Published online: 18 November 2006

Abstract Many disease processes involve alterations in the chemical makeup of tissue. Synchrotron-based infrared (IR) and X-ray fluorescence (XRF) microscopes are becoming increasingly popular tools for imaging the organic and trace metal compositions of biological materials, respectively, without the need for extrinsic labels or stains. Fourier transform infrared microspectroscopy (FTIRM) provides chemical information on the organic components of a material at a diffraction-limited spatial resolution of 2–10 μm in the mid-infrared region. The synchrotron X-ray fluorescence (SXRF) microprobe is a complementary technique used to probe trace element content in the same systems with a similar spatial resolution. However to be most beneficial, it is important to combine the results from both imaging techniques on a single sample, which requires precise overlap of the IR and X-ray images. In this work, we have developed a sample substrate containing a gold grid pattern on its surface, which can be imaged with both the IR and X-ray microscopes. The substrate consists of a low trace element glass slide that has a gold grid patterned on its surface, where the major and minor parts of the grid contain 25 and 12 nm gold, respectively. This grid pattern can be imaged with the IR microscope because the reflectivity of gold differs as a function of thickness. The pattern can also be imaged with the SXRF microprobe because the Au fluorescence intensity changes with gold thickness. The tissue sample is placed on top of the patterned substrate. The grid pattern's IR reflectivity image and the gold SXRF image are used as fiducial markers for spatially overlapping the IR and SXRF images from the tissue. Results show that IR and X-ray images can be correlated precisely, with a spatial resolution of less than one pixel (i.e., 2–3 microns). The development of this new tool will be presented along with applications to paraffin-embedded metalloprotein crystals, Alzheimer's disease, and hair composition.

Keywords Infrared microspectroscopy · X-ray fluorescence microprobe · Nanopatterning · Metals · Tissues

Abbreviations

(IR)	infrared
(FTIRM)	fourier transform infrared microspectroscopy
(SXRF)	synchrotron X-ray fluorescence
(AFM)	atomic force microscopy
(AD)	Alzheimer's disease

L. M. Miller (✉) · Q. Wang · R. J. Smith · H. Zhong
National Synchrotron Light Source,
Brookhaven National Laboratory,
Bldg 725 D, 75 Brookhaven Avenue, Upton, NY 11973, USA
e-mail: lmiller@bnl.gov

D. Elliott
Instrumentation Division,
Brookhaven National Laboratory,
Upton, NY, USA

J. Warren
Center for Functional Nanomaterials,
Brookhaven National Laboratory,
Upton, NY, USA

Introduction

Many disease processes involve alterations in the chemical makeup of tissue. Fourier transform infrared microspectros-

copy (FTIRM) and synchrotron X-ray fluorescence (SXRF) microprobes are becoming increasingly popular tools for imaging the organic and trace metal compositions of biological materials without the need for extrinsic labels or stains. Coupled to a synchrotron infrared (IR) source, FTIRM provides chemical information on the organic components of a tissue such as proteins, lipids, nucleic acids, and carbohydrates, at a diffraction-limited spatial resolution of 2–10 μm in the mid-infrared region [1]. FTIRM is very sensitive to protein secondary structure in tissue as well, where the frequency of the amide I band, assigned to the amide (>C=O) backbone of the protein, has a different absorption maximum for α-helical (~1655 cm^{-1}), β-sheet (~1630 cm^{-1}), and extended coil (~1645 cm^{-1}) proteins [2, 3]. For example, the structure of misfolded protein aggregates has been identified in the brain tissue of Alzheimer's disease patients [4–6] and infectious prion proteins have been characterized in scrapie [7–10]. In addition to protein structure, variations in bone composition have been observed in osteoporosis [11–13], osteopetrosis [14], and osteoarthritis [15]. In heart disease, altered lipid and collagen content and structure in the myocardium have been seen [16], which were partially normalized by losartan treatment [17].

The synchrotron X-ray fluorescence (SXRF) microprobe is a complementary technique used to probe trace elements with sensitivities in the sub-mg kg^{-1} range and a spatial resolution similar to FTIRM (2–10 μm) [18]. Because of the low power deposition that X-rays provide and the ability to conduct the analyses in air, these analyses can be done nondestructively on a much wider array of sample types, in particular relatively fragile biological samples. For example, alterations in trace metals such as Fe, Cu, and Zn have been observed in neurological diseases such as Parkinson's disease, amylotrophic lateral sclerosis, Alzheimer's disease, prion diseases [5, 19–21] and cancer [22]. Environmental toxins have also been imaged in human tissue, such as elevated levels of methyl mercury [23] and lead [24] in hair.

In many disease states and environmental contaminations, both the organic and metal ion compositions are altered. Yet most of the abovementioned studies utilize either FTIRM or SXRF microprobes, but not both, and therefore examine only one aspect of the disease, resulting in missing information on the relationship between the changes in the organic and metal contents, which play a vital role in understanding the origins of the disease. This is likely due to technical difficulties such as sample preparation, sample substrates, and image registration. In this work, we present the development of a sample substrate that contains a gold grid pattern on its surface, which can be imaged with both IR and X-ray microscopes. The tissue sample is placed on this substrate and the gold pattern is used as a fiducial marker to co-register the FTIRM and SXRF microprobe images. The development of this new tool will be presented along with applications to paraffin-embedded metalloprotein crystals, Alzheimer's disease, and hair composition.

Materials and methods

Nanopatterning

Low trace element Suprasil 2 fused silica disks (1.5" diam x 0.063" thick) were purchased from Heraeus Optics (Buford, GA, USA). Gold shot (99.9999% purity) was purchased from ESPI. To produce the gold pattern on the disk, a 13 nm layer of Au was first evaporated onto the fused silica disk, where the thickness was measured by a quartz crystal monitor (error was±2 nm). After spin-coating Shipley 1881 positive photoresist over the evaporated Au, a 4″ chrome-on-glass contact mask (Advanced Reproduction Corp., Andover, MA, USA) was placed on the disk, which was exposed to 350–450 nm UV light (Oriel 27240 exposer with 350 watt Hg lamp; Newport, Irvine, CA, USA) for 45 s to activate the photoresist. The exposed photoresist was removed by submerging the disk for 30 s in a 1:1 ratio of MF-312 developer and water followed by a water rinse. The Au that was not protected by the patterned photoresist was then removed with a 3:1 HCl:HNO_3 solution. The remaining photoresist was removed with acetone, leaving only the major part of the pattern with a thickness of 13 nm. A second layer of Au was evaporated over the entire disk at a thickness of 12 nm, making the final grid thickness 12 nm, and the remainder of the disk was 25 nm. A schematic showing the nanopatterning process can be seen in Fig. 1.

Sample preparation

Metalloprotein distribution Lyophilized horse heart myoglobin protein (Sigma, St. Louis, MO, USA) was suspended in melted paraffin wax and allowed to cool. Sections from the resulting paraffin block were cut with a disposable stainless steel blade on a cryomicrotome (model 2488, IEC, Needham Heights, MA, USA) to a thickness of 7 μm and deposited onto a patterned slide.

Alzheimer's disease The brain of a PDAPP mouse model of AD was snap-frozen in liquid nitrogen and stored at −80 °C until processing. A cryomicrotome (IEC) was used to cut 10 μm-thick sections at −15 °C, which were deposited onto the patterned slide. The tissue was allowed to dry and was then stained with Thioflavin S, a green fluorochrome (excitation: 430 nm; emission: 550 nm) that binds to

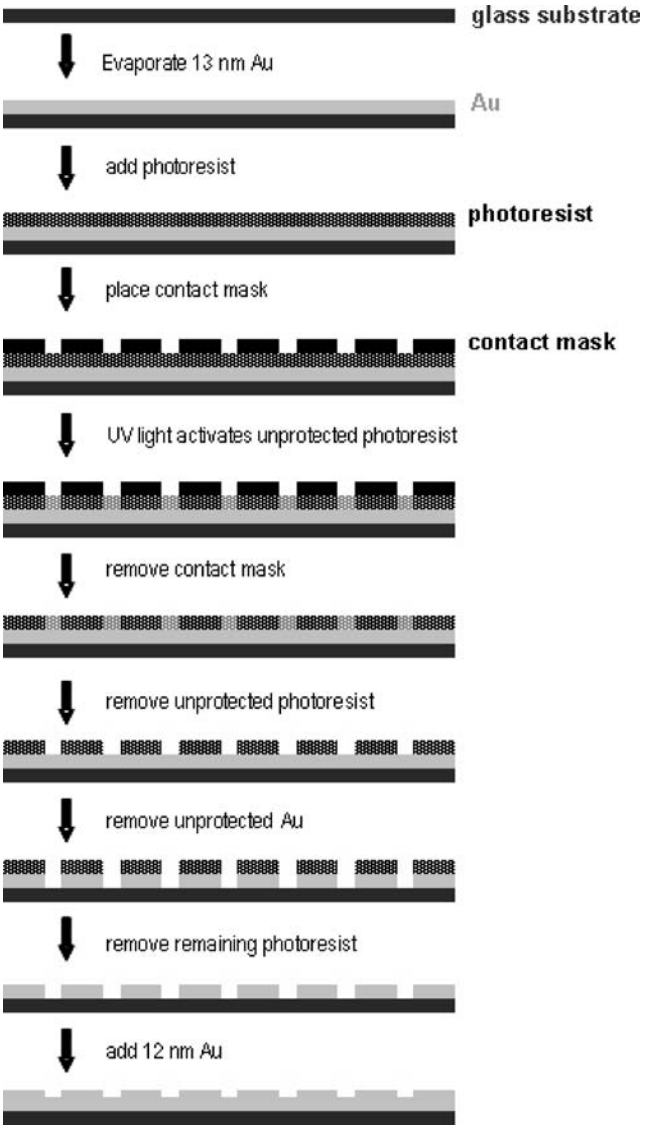

Fig. 1 Schematic of the gold grid patterning process

amyloid plaques in AD. The detailed procedure has been described previously [5, 25].

Hair composition A tuft of wetted human hair (~10 hairs, 1 cm in length) was embedded in melted paraffin wax and allowed to cool. Cross-sections of the embedded hair were cut with a disposable stainless steel blade on a cryomicrotome (IEC) at room temperature to a thickness of 7 μm and deposited onto a patterned slide.

Data collection and analysis

Fourier transform infrared microspectroscopy (FTIRM) FTIR spectra and images were collected at beamline U10B at the National Synchrotron Light Source, Brookhaven National Laboratory (Upton, NY, USA). A Thermo Nicolet Magna 860 FTIR spectrometer, coupled to a Continuμm IR microscope (Thermo Nicolet, Madison, WI, USA) was used with synchrotron light as the infrared source. The microscope was equipped with a matching 32× Schwarzschild objective/condenser pair, a motorized x–y mapping stage, an adjustable rectangular aperture, and a mercury cadmium telluride (MCT-A) detector. The IR microscope stage was raster-scanned through the area with a step size of 4 μm / pixel for the hair and myoglobin data and 10 μm / pixel for the AD data using Atlμs software (ThermoNicolet). At each point, an absorbance spectrum was recorded in trans-reflectance mode, i.e., the IR beam passed through the sample, reflected off of the gold surface, and passed through the sample again. Each spectrum was collected in the mid-infrared spectral range (4000–800 cm^{-1}) with a spectral resolution of 8 cm^{-1} and 64 scans co-added. The IR beam (aperture) size was 10×10 μm. The background spectrum was collected from a clean area of the patterned slide, and the final spectra were recorded in log (1/*R*) format.

For each sample, chemical images were generated by calculating specific peak height or area ratios at each pixel of the image. In the metalloprotein and hair examples, an image of protein distribution was determined by integration of the amide I (>C=O) protein peak from 1600–1700 cm^{-1}. A single-point linear baseline at 1800 cm^{-1} was used to correct for the decaying synchrotron beam current over time. For the AD study, the distribution of aggregated β-sheet protein in the tissue was imaged by calculating the ratio of the peak intensities at 1630 cm^{-1} (β-sheet) and 1655 cm^{-1} (α-helix). A single-point linear baseline at 1800 cm^{-1} was used to correct for the decaying synchrotron beam current over time. The grid pattern on the substrate was identified by plotting an area map in the spectral region of 3800–4000 cm^{-1} using CytoSpec software. The baseline of each spectrum in this spectral region is dependent upon the IR reflectivity of the substrate, which is ~85% on the grid lines and 100% elsewhere.

Synchrotron X-ray fluorescence (SXRF) microprobe SXRF microprobe experiments were carried out at beamline X26A at the National Synchrotron Light Source, Brookhaven National Laboratory (Upton, NY, USA) and beamline 13ID at the Advanced Photon Source, Argonne National Laboratory (Argonne, IL, USA). At X26A, the synchrotron X-ray beam was tuned to 12.1 keV using a Si(111) channel-cut monochromotor. The incident beam was then collimated to 350 μm×350 μm and then focused using Rh-coated Kirkpatrick–Baez focusing optics to an approximate size of 5 μm×8 μm. This provided an X-ray flux of approximately 10^9 photons/s on the sample. The sample was placed at a 45° angle to the incident X-ray beam, and X-ray fluorescence was detected with a nine-element Ge detector

(Canberra, Meriden, CT, USA) oriented at 90° to the incident beam, which collects a solid angle of approximately 0.12 steradians. A light microscope objective (M Plan Apo 5X, Mitutoyo, Aurora, IL, USA) was coupled to a digital CCD camera for sample viewing in transmission or reflection geometries. A similar SXRF set-up was used at beamline 13-ID. Thioflavin S fluorescence was viewed using an epifluorescence module that was mounted between the light microscope objective and the CCD camera [26].

A predefined area matching the area measured by FTIRM was scanned with step size of 5 μm / pixel for the AD sample and 4 μm / pixel for the hair and myoglobin samples. At each pixel, fluorescence counts for the metals of interest were extracted from energy-dispersive spectra by integrating the respective X-ray emission lines (Fe K_α, Cu K_α, Zn K_α). Data were collected for 1, 2, and 10 s/pixel for the Au grid, myoglobin, and hair samples, respectively, at NSLS beamline X26A. AD data were collected at beamline 13ID by integrating for 1 s / pixel.

Overlapping and correlations In order to overlap the gold grid images from FTIRM and the SXRF microprobe, a custom Matlab routine was developed using the Image Processing Toolbox. The grid pattern was determined by the change in IR reflectivity or X-ray fluorescence, and a binary (black/white) grid image generated. Coordinate shifts were calculated and the binary images were superimposed. The outer edges of the resulting image were cropped such that the final image contained both FTIRM and SXRF data. Correlation analysis can be performed by plotting (x,y) pairs from the FTIRM and SXRF data at each pixel and calculating a correlation coefficient (R^2 value).

Results and discussion

Substrate characterization Figure 2a illustrates a schematic of the gold grid pattern on the glass substrate. From light microscopy, it can be seen that the width of the gold bar is 15 μm and the pitch (distance between bars) is 200 μm. In order to assess the thickness of the gold pattern, atomic force microscopy was performed (Fig. 2b). A line scan from clean glass to the grid bar showed that the step up was approximately 12 nm, where the sharpness of the step was <1 μm. A line scan from the grid bar to the open area showed that the step jump was approximately 15 nm, where the sharpness of the step edge was <1 μm. Thus, the thickness of the gold bar was confirmed to be 12 nm, and the gold on the remainder of the disk was approximately 27 nm thick.

The relationship between Au reflectivity and thickness can be seen in Fig. 3a. Between 10 and 20 nm of Au, there is a sharp increase in reflectivity from 10% to 90%. Thus, the Au thickness for the grid pattern was chosen to be 12–15 nm, which provides sufficiently high reflectivity to collect FTIR spectra but also a reflectivity that is low enough to differentiate the thick (25 nm, 100% reflectivity) from the thinner Au. The FTIR spectra for 25 and 15 nm gold are shown in Fig. 3b. As can be seen, the Au reflectivity is flat over the spectral range from 4000–1000 cm^{-1}. An IR reflection image from 3800–4000 cm^{-1} for the patterned substrate shows that the bars of the grid are clearly visible due to the reduced IR reflectivity, where the sharpness of the edge is 2–3 μm (Fig. 3c).

For the SXRF microprobe, the intensity of the gold fluorescence signal was proportional to the thickness of the gold (Fig. 4a). The thickness of the grid pattern was 12 nm,

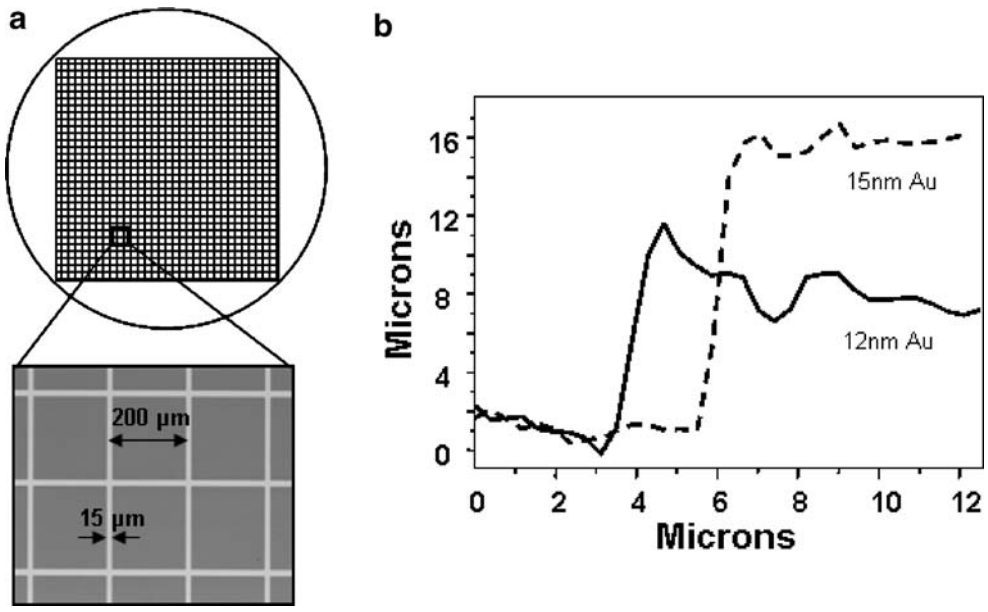

Fig. 2a, b **a** Schematic (*top*) and light microscope image (*bottom*) of the patterned substrate. The bar width is 15 μm and the pitch is 200 μm. **b** AFM line maps from clean glass to the gold bar (*solid*) and from the bar to the open area (*dashed*)

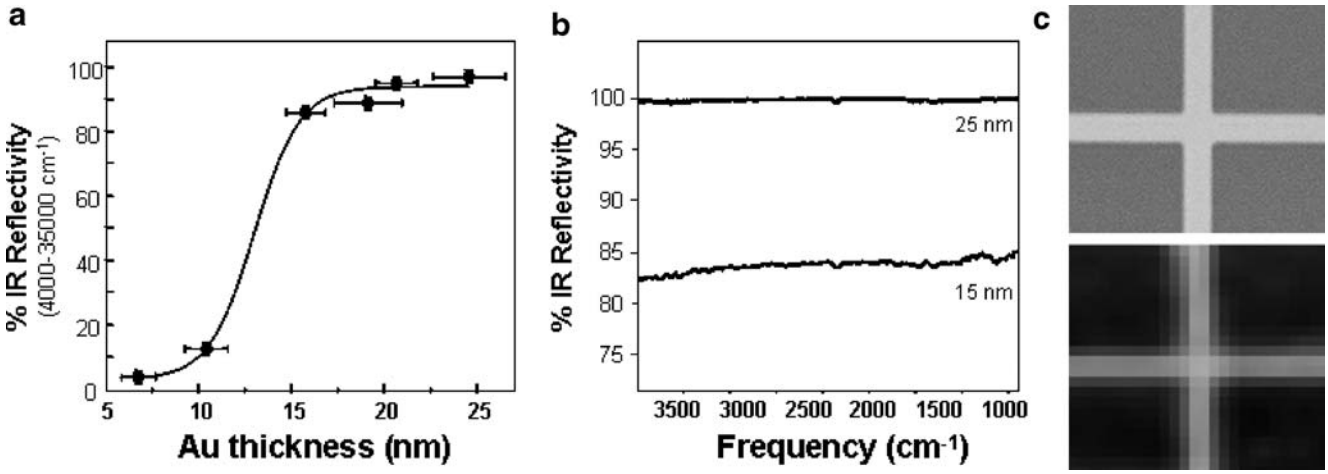

Fig. 3a–c **a** Infrared reflectivity of gold as a function of thickness. The final grids were produced with a bar thickness of 12 nm (~85% reflectivity), and the remaining part of the grid was 25 nm (100% reflectivity). **b** IR reflectivity spectra of 15 nm and 25 nm gold from 4000 to 1000 cm^{-1}. **c** FTIRM image of the patterned gold grid, where *gray* indicates low reflectivity and *black* indicates high reflectivity

which was approximately half the thickness of the remainder of the substrate (25 nm). The integrated gold fluorescence intensity of the grid (340 counts) was also approximately half of the integrated intensity from the remainder of the substrate (750 counts) (Fig. 4b). Similar to the FTIRM results, the sharpness of the bar edge was 2–3 μm, as can be seen in the Au SXRF microprobe image of the grid (Fig. 4c). These findings showed that both the IR and X-ray microscopes are sensitive to the gold pattern on the substrate.

Correlation of metal and organic composition In order to test the ability to superimpose FTIRM and SXRF images using the grid pattern, crystals of a lyophilized metalloprotein (i.e., myoglobin) were embedded in paraffin, microtomed, and a thin section was deposited on the patterned substrate. The location of the protein in the paraffin was determined with FTIRM, while the location of the iron in the thin section was determined with the SXRF microprobe. Since the iron is covalently bound to the protein, the two images should "perfectly" correlate, and thus provide a measure of the precision of the technique.

Figure 5a shows a light microscope image of the myoglobin crystals embedded in the paraffin section, where the location of the crystals is evident based on their red color. The Au reflectivity (FTIRM) and Au SXRF images can be seen in Fig. 5b and 5c, respectively. Note that the sample absorbance can interfere with the FTIRM reflectivity data so that the entire grid pattern is not visible. However, image overlap only requires one cross-bar, which is indicated by the black arrow. It should be noted that, in some cases, the visible light image from the IR data collection is more desirable for image overlap than the IR reflectivity image. In FTIRM imaging, the visible light path for sample illumination is identical to the infrared light path for data collection, i.e., the same reflective optics are used. Thus, the visible light and infrared images are perfectly correlated. However, for SXRF imaging this is not the case.

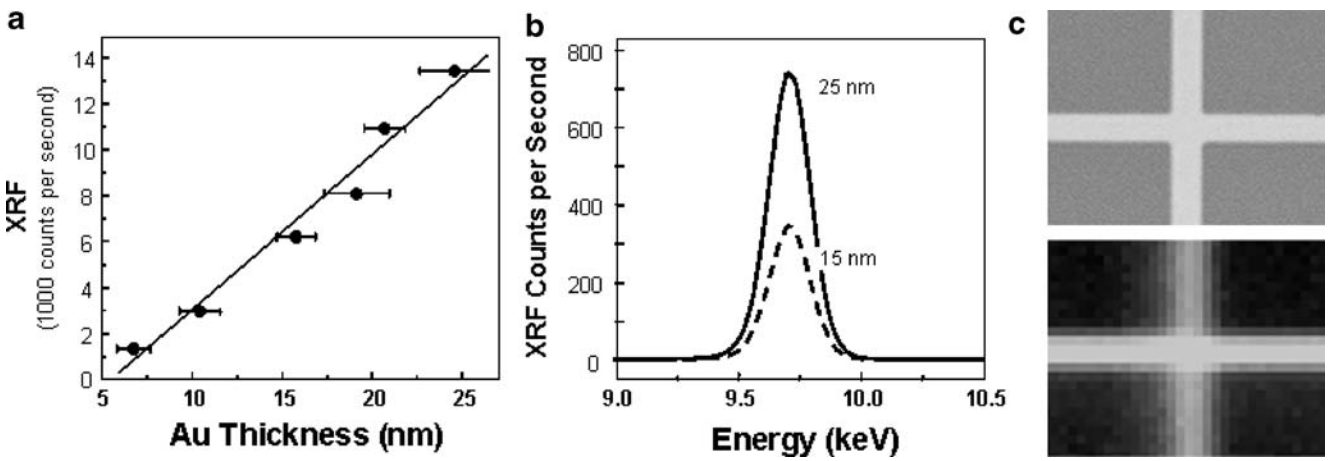

Fig. 4a–c **a** SXRF intensity of gold as a function of thickness. **b** SXRF spectra of 15 nm (*dashed*) and 25 nm (*solid*) gold from 9 to 10.5 keV. **c** SXRF image of the patterned gold grid, where *gray* indicates low fluorescence counts and *black* indicates higher counts

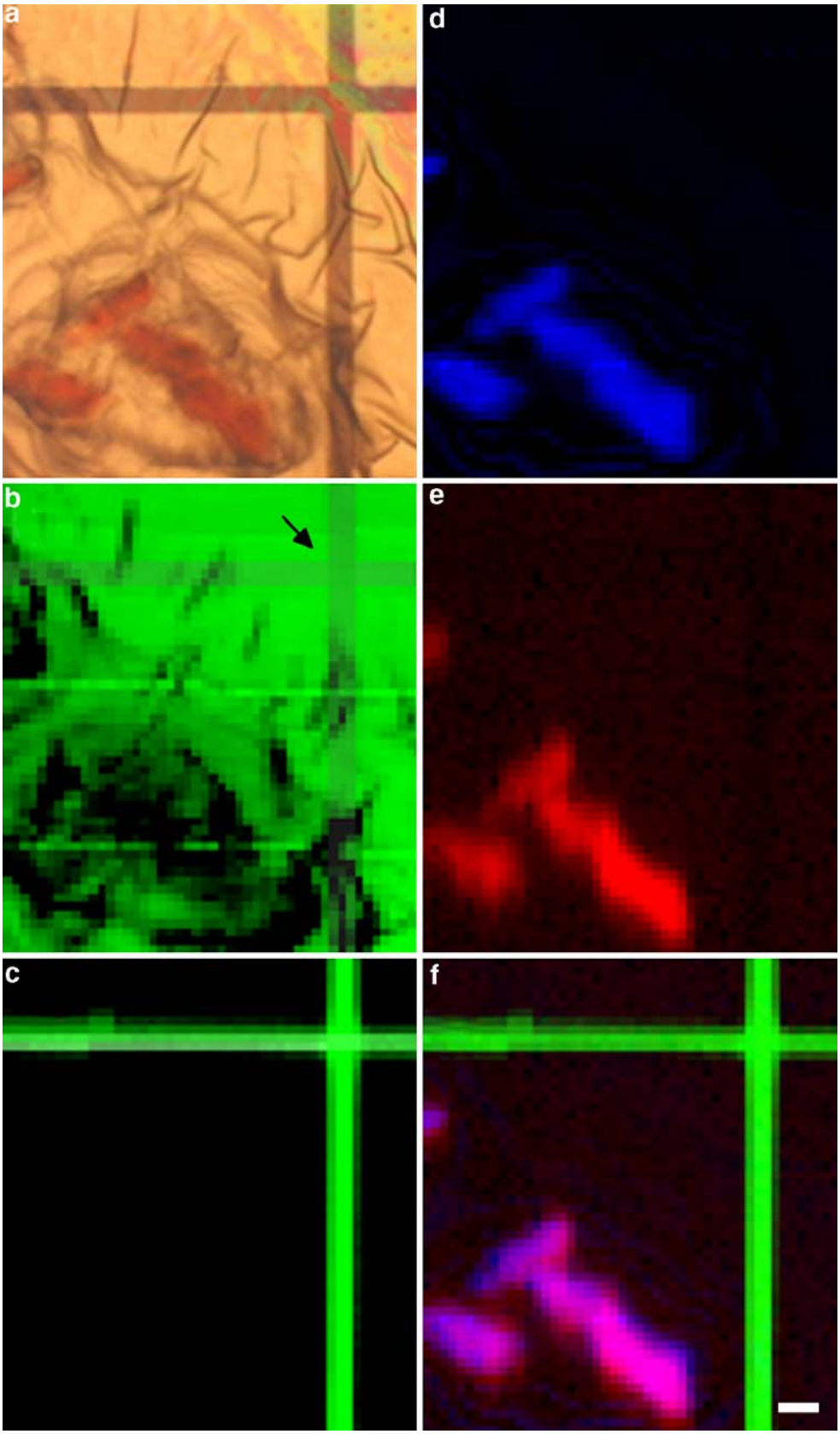

Fig. 5a–f **a** A biological copolymer, consisting of lyophilized myoglobin embedded in paraffin, under visible light illumination. **b** FTIRM reflectivity image of the Au grid. **c** Au SXRF image of the Au grid. **d** FTIRM image of the protein content in the copolymer, generated by plotting the amide I peak area from 1600 to 1700 cm^{-1}. **e** SXRF microprobe image of iron content in the copolymer. **f** A 24-bit RGB color image illustrating the correlation of the protein from FTIRM (blue channel) and Fe content from SXRF microprobe (red channel) in the tissue. The gold grid pattern from the SXRF microprobe is placed in the green channel. The scale bar for all images is 20 μm

Visible light illumination and sample magnification is performed through a glass microscope objective. The focused X-ray beam is then positioned at the focus spot (e.g., the crosshair) of the light microscope image. However, if the visible light image and X-ray beam are not precisely overlapped, then the resulting SXRF images will be shifted from the light microscope images. Moreover, any motion in the X-ray beam or the visible light optics during data collection can cause a mismatch in the overlap. Since the X-ray beam is not visible during data collection, it is not obvious that this has occurred. By using an X-ray-sensitive grid pattern, the position of the X-ray beam is always accurately known.

The FTIRM image of the amide I band (1600–1700 cm^{-1}), indicative of protein, can be seen in Fig. 5d. Since the chemical structure of paraffin lacks any amide bonds, there is no absorbance overlap in this spectral region. The iron SXRF microprobe image of the same area can be seen in Fig. 5e. The FTIRM and SXRF images were superimposed by overlapping the gold grid patterns. In this example, the FTIRM image was shifted by 16 μm to the right in the horizontal direction and 4 μm down in the vertical direction to correspond to the coordinates of the SXRF image. The outer edges of both images were cropped so that only data containing IR and SXRF information were included. As can be seen in Fig. 5f, an excellent correlation was observed between the protein and iron images, where a subpixel precision of 2–3 μm was found.

Application to Alzheimer's disease The brain in Alzheimer's disease (AD) is characterized by the presence of amyloid plaques, which are aggregates of the misfolded amyloid-beta (Abeta) protein. In its normal form, Abeta is primarily an α-helical protein, where the peak frequency of the IR amide I band is 1655 cm^{-1}. When Abeta misfolds, it forms a β-sheet structure and then aggregates, shifting the amide I peak frequency to ~1630 cm^{-1}. Thus, FTIRM can be used to image amyloid plaques in AD brain based on this shift in frequency. Figure 6a shows epifluorescence images of a thin section of AD brain that has been stained with thioflavin S and deposited onto the gold-patterned substrate. The gold pattern is visible in the image. The bright green areas show thioflavin S fluorescence, which is associated with amyloid plaques.

By measuring the IR reflection from 3800–4000 cm^{-1}, where the tissue does not absorb IR light, the FTIRM image of the gold grid can been seen (Fig. 6b). FTIRM spectra from a region of healthy tissue and a plaque-containing region can be seen in Fig. 6g. The shift in the amide I band to lower frequency distinguishes the plaque-like protein structure. The FTIRM image of the plaques, generated by calculating the amide I peak height ratio of 1630 cm^{-1} (aggregated β-sheet) to 1655 cm^{-1} (α-helix), shows that the regions of misfolded, aggregated protein correlate well with the thioflavin S staining (Fig. 6d).

Recently, the formation of amyloid plaques in AD has been associated with metal accumulation in the brain, such as Fe, Cu, and Zn [5, 27]. Similar observations have been made for other neurodegenerative diseases such as Parkinson's disease and amyotrophic lateral sclerosis [28]. In order to understand this process, it is beneficial to image both the metal ion distribution and plaque location in identical samples. In this study, the distribution of Zn will be presented, but a further discussion of Cu, Fe, and Ca involvement can be found elsewhere [5]. The Au and Zn SXRF microprobe images are shown in Fig. 6c and 6e, respectively, for the same sample imaged by FTIRM in Fig. 6d. The SXRF image was cropped in both the horizontal and vertical directions such that the FTIRM and SXRF grid patterns overlap. As can be seen from Fig. 6e, "hot spots" of Zn are evident, which appear to co-localize with the locations of some amyloid plaques (from Fig. 6d). Sample SXRF spectra from the healthy and plaque-containing regions of tissue (Fig. 6h) and the resulting RGB image confirm this correlation (Fig. 6f). These data suggest that Zn ions may play a role in amyloid formation in AD, in support of in vitro [29] and cell culture [30] studies. However, there are several other areas where amyloid is observed, but the Zn concentration is not elevated. These findings indicate that amyloid formation can be present without significant Zn accumulation, and may suggest that amyloid plaques need to be a sufficient size, density, and/or concentration before Zn binds to them.

Application to hair composition FTIRM has been shown to be a unique method for examining the chemical makeup of hair. Especially with the high resolution of a synchrotron-based IR source, it is possible to separately analyze the different regions of the hair cross-section, i.e., the cuticle, cortex, and medulla. It has been used to study drug abuse by examining the uptake of drugs into the medulla—the central core—of human hair. This technique eliminates the question of externally contaminated hair by analyzing only that portion of the hair that is formed from within the root, where ingested material would be transported [31, 32]. FTIRM has also been used to study the effects of bleaching and coloring on different regions of the hair [33], and the process of ancient mummification [34].

Hair analysis has also frequently been used to study environmental metal contaminants such as methyl mercury uptake from eating contaminated fish [23], lead poisoning in children from drinking water pipes [24], and lead accumulation in smelter workers [35]. Yet to date, very little work has been done comparing the organic composition of the hair with the propensity for metal uptake. By combining FTIRM and the SXRF microprobe, this can be accomplished.

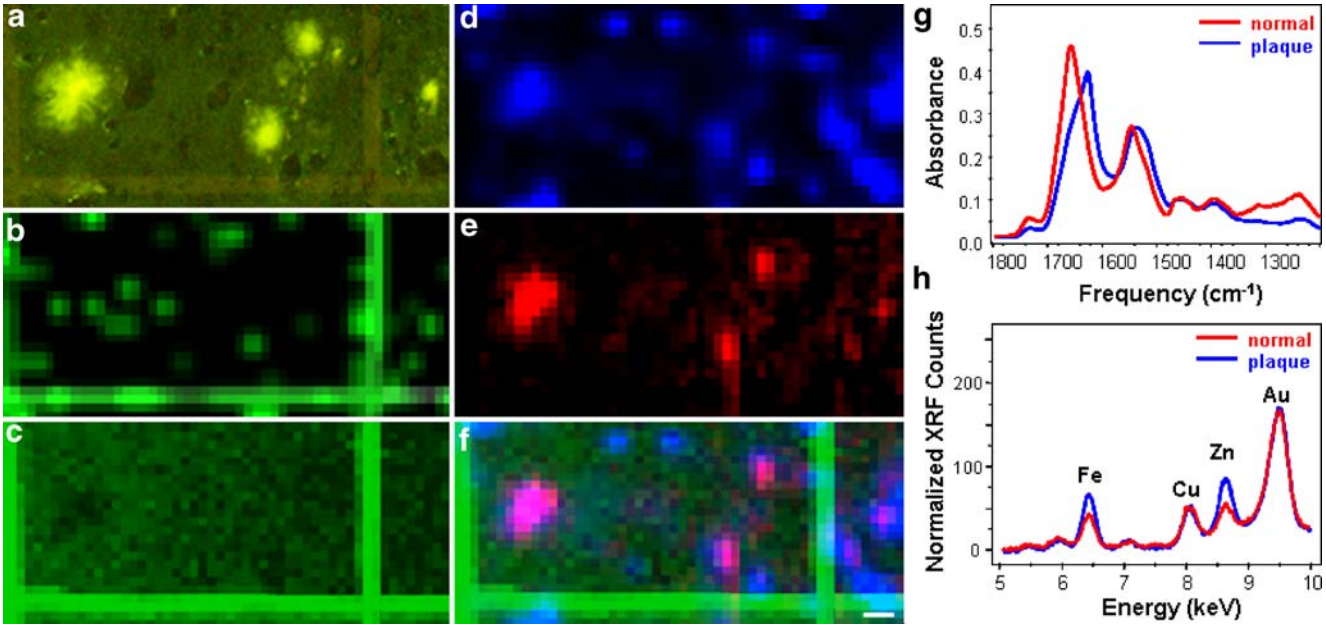

Fig. 6a–h **a** Alzheimer's diseased brain tissue stained with thioflavin S under fluorescence illumination. With thioflavin S staining, amyloid plaques appear green. **b** IR reflectivity image of the Au grid. **c** Au SXRF microprobe image of the Au grid. **d** FTIRM image of AD plaques, i.e., misfolded protein content, generated by plotting a peak height ratio of 1630 cm^{-1} (β-sheet) / 1655 cm^{-1} (α-helix). **e** SXRF microprobe image of zinc content in the brain tissue. **f** A 24-bit RGB color image illustrating the correlation of the amyloid plaques from FTIRM (blue channel) and Zn content from the SXRF microprobe (red channel) in the tissue. The gold grid pattern from the SXRF microprobe is placed in the green channel. **g** FTIRM spectra and **h** SXRF microprobe spectra from a normal (*red*) and amyloid-containing (*blue*) region of brain tissue. The scale bar for all images is 20 μm

Figure 7a shows a cross-section of a human hair that has been embedded in paraffin wax, microtomed to a thickness of 7 μm, and deposited onto a gold-patterned substrate. The grid pattern is clearly visible under the light microscope. A typical FTIRM spectrum from the hair can be seen in Fig. 7g, which shows that the main component of the hair is protein. FTIRM analysis of the amide I protein band (1600–1700 cm^{-1}) can be seen in Fig. 7d. The protein distribution is lower in the medulla, and relatively uniform throughout the remainder of the hair. For the SXRF microprobe images, the Cu image shows an elevated amount of Cu in the cuticle of the hair (Fig. 7e). This can also be seen by comparing individual SXRF spectra (Fig. 7h). By overlaying the FTIRM and SXRF images, results show that the elevated ring of Cu is outside the protein distribution (Fig. 7f). These findings indicate that the protein content is inversely correlated with the Cu content in the hair.

Since the cuticle is the outermost layer of the hair, this suggests that the elevated copper content in the cuticle is due to exogenous copper binding. Prior studies on copper content in hair have shown that damage to the cuticle of the hair can increase the cysteic acid and anionic sulfonate groups in keratin, which enhance copper adsorption [36]. Conversely, if the metabolic levels of copper were elevated in the body, this would most likely be transported to the hair through the medulla, which was not observed in this study.

Limitations and variations In the experiments described here, both FTIRM and the SXRF microprobe are applied to the same sample. Thus, an important consideration is the selection of an appropriate sample thickness that will be acceptable for both techniques. For FTIRM experiments performed in reflection mode, biological tissue thicknesses are limited to a range of approximately 5–15 μm. For the SXRF microprobe, the acceptable thickness range is broader, i.e., approximately 10–50 μm for a lateral spatial resolution of 5–10 μm. However, in most tissue samples, trace metal content is on the order of 10–100 ppm, making thicker samples desirable. Therefore, in most cases, it is best to choose the thickest possible section for FTIRM, which is sufficient for the SXRF microprobe.

Variations in the substrate and grid material were also examined. Typical IR-transparent salt crystals (e.g., CaF_2, BaF_2, KBr) cannot be used as sample substrates because of the strong X-ray fluorescence from these materials. Diamond substrates are a viable alternative, but are costly and often contain high concentrations of trace metals. Besides gold, aluminum is also a common IR-reflective metal. However, it cannot be used do to the low energy of its X-ray

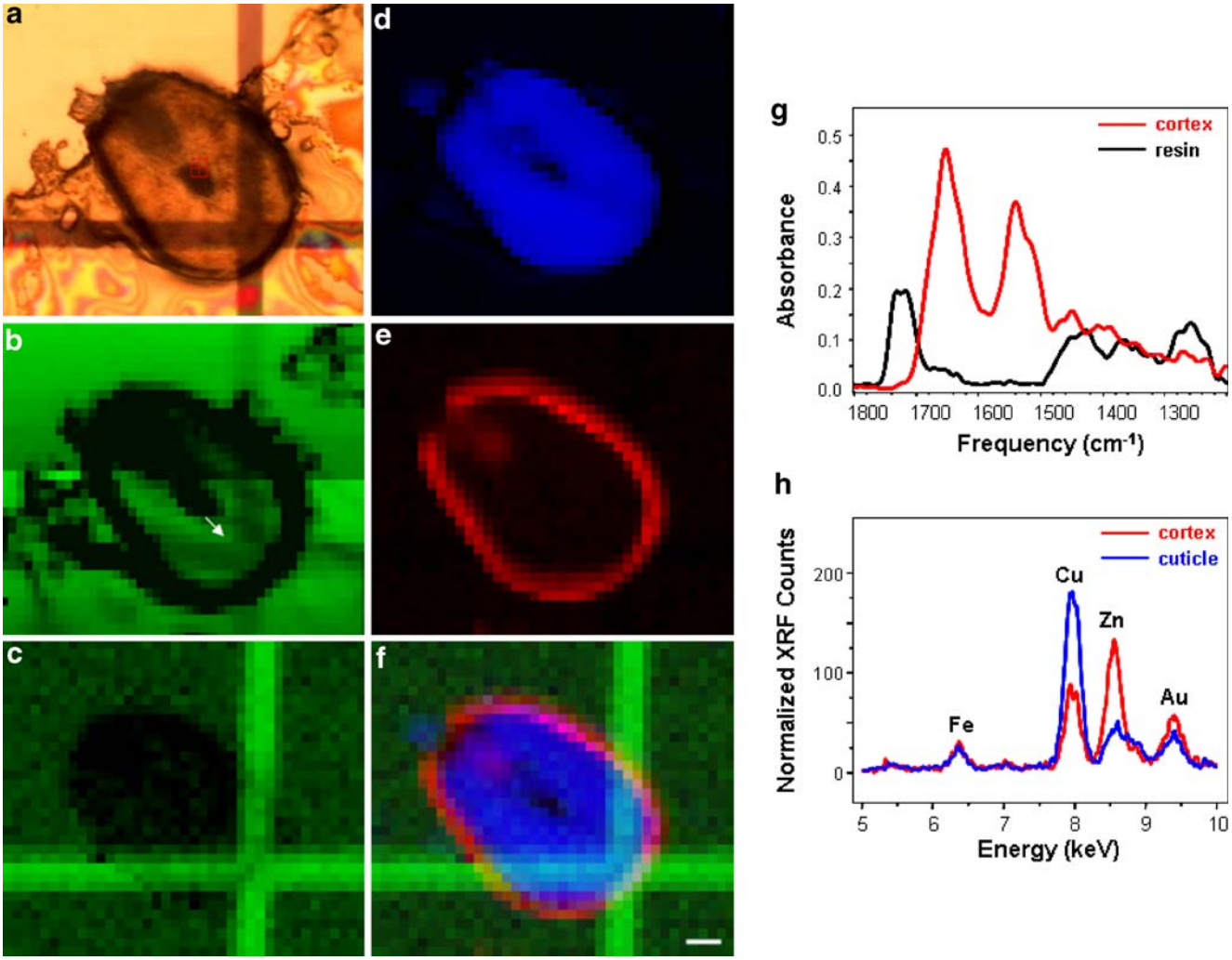

Fig. 7a–h **a** Cross-section of human hair under visible light illumination. **b** FTIRM reflectivity image of the Au grid. **c** Au SXRF microprobe image of the Au grid. **d** FTIRM image of the protein content in the hair, generated by plotting the amide I peak area from 1600 to 1700 cm^{-1}. **e** SXRF microprobe image of copper content in the hair. **f** A 24-bit RGB color image illustrating the correlation of the protein from FTIRM (blue channel) and Cu content from the SXRF microprobe (red channel) in the tissue. The gold grid pattern from the SXRF microprobe is placed in the green channel. **g** FTIRM spectra from the cortex of the hair (*red*) and embedding resin (*black*). **h** SXRF microprobe spectra from the cortex (*red*) and cuticle (*blue*) of the hair. Scale bar for all images is 20 μm

fluorescence. Other metals, such as titanium and chromium, have been tested and work reasonably well. It is important to choose a metal that is not present in the sample, and does not have an interfering fluorescence emission line.

Conclusions

In summary, synchrotron-based infrared and X-ray fluorescence microscopes are complementary tools for imaging the organic and trace metal compositions of biological materials, respectively, without the need for extrinsic labels or stains. However, in order to directly correlate organic composition and trace metal content, it is important to precisely overlap the IR and X-ray images. We have developed a gold-patterned sample substrate, where the grid pattern is sensitive to both X-ray and infrared light, and the resulting images can be used as fiducial markers to spatially overlap the FTIRM and SXRF images from the tissue. We show that FTIRM and SXRF images can be correlated precisely, with a spatial resolution of less than one pixel, i.e., 2–3 microns. By combining FTIRM and SXRF microprobe on the same sample utilizing this sample substrate, a more complete picture of many disease states and exposure to environmental contaminants can be achieved by directly correlating the organic and trace metal ion distributions in the tissue.

Acknowledgements The authors would like to thank Tony Lanzirotti and Bill Rao at NSLS Beamline X26A and Matt Newville and Steve Sutton at APS Beamline 13-ID for their support with beamline operation and data collection. This work was supported by the National Institutes of Health Grant R01-GM66873. The NSLS and APS are supported by the United States Department of Energy, Office of Science, Office of Basic Energy Sciences, under contracts DE-AC02-98CH10886 and W-31-109-Eng-38, respectively.

References

1. Miller LM, Dumas P (2006) Chemical imaging of biological tissue with synchrotron infrared light. Biochim Biophys Acta 1758(7):846–57
2. Byler DM, Susi H (1986) Examination of the secondary structure of proteins by deconvolved FTIR spectra. Biopolymers 25:469–487
3. Susi H, Byler DM, Purcell JM (1985) Estimation of beta-structure content of proteins by means of deconvolved FTIR spectra. J Biochem Biophys Methods 11:235–240
4. Choo LP, Wetzel DL, Halliday WC, Jackson M, LeVine SM, Mantsch HH (1996) In situ characterization of beta-amyloid in Alzheimer's diseased tissue by synchrotron Fourier transform infrared microspectroscopy. Biophys J 71:1672–1679
5. Miller LM, Wang Q, Telivala TP, Smith RJ, LanzirottiA, Miklossy J (2006) Synchrotron-based infrared and X-ray imaging shows focalized accumulation of Cu and Zn co-localized with beta-amyloid deposits in Alzheimer's disease. J Struct Biol 155:30– 37
6. Gallant M, Rak M, Szeghalmi A, Del Bigio MR, Westaway D, Yang J, Julian R, Gough KM (2006) Focally elevated creatine detected in amyloid precursor protein (APP) transgenic mice and Alzheimer disease brain tissue. J Biol Chem 281:5–8
7. Kneipp J, Lasch P, Baldauf E, Beekes M, Naumann D (2000) Detection of pathological molecular alterations in scrapie-infected hamster brain by Fourier transform infrared (FT-IR) spectroscopy. Biochim Biophys Acta 1501:189–199
8. Kneipp J, Miller LM, Joncic M, Kittel M, Lasch P, Beekes M, Naumann D (2003) In situ identification of protein structural changes in prion-infected tissue. Biochim Biophys Acta 1639:152–158
9. Kneipp J, Miller LM, Spassov S, Sokolowski F, Lasch P, Beekes M, Naumann D (2004) Scrapie-infected cells, isolated prions, and recombinant prion protein: a comparative study. Biopolymers 74:163–167
10. Wang Q, Kretlow A, Beekes M, Naumann D, Miller L (2005) In situ characterization of prion protein structure and metal accumulation in scrapie-infected cells by synchrotron infrared and X-ray imaging. Vib Spectrosc 38:61–69
11. Huang RY, Miller LM, Carlson CS, Chance MR (2002) Characterization of bone mineral composition in the proximal tibia of cynomolgus monkeys: effect of ovariectomy and nandrolone decanoate treatment. Bone 30:492–497
12. Huang RY, Miller LM, Carlson CS, Chance MR (2003) In situ chemistry of osteoporosis revealed by synchrotron infrared microspectroscopy. Bone 33:514–521
13. Ruppel ME, Burr DB, Miller LM (2006) Chemical makeup of microdamaged bone differs from undamaged bone. Bone 39 318–324
14. Miller LM, Vairavamurthy V, Chance MR, Mendelsohn R, Paschalis EP, Betts F, Boskey AL (2001) In situ analysis of mineral content and crystallinity in bone using infrared micro-spectroscopy of the nu(4) PO(4)(3-) vibration. Biochim Biophys Acta 1527:11–19
15. Miller LM, Novatt JT, Hamerman D, Carlson CS (2004) Alterations in mineral composition observed in osteoarthritic joints of cynomolgus monkeys. Bone 35:498–506
16. Wang Q, Sanad W, Voigt A, Klingel K, Kandolf R, Stangl K, Baumann G, Miller LM (2005) Infrared imaging of compositional changes in inflammatory cardiomyopathy. Vib Spectrosc 38:217–222
17. Gough KM, Zelinski D, Wiens R, Rak M, Dixon IMC (2003) Fourier transform infrared evaluation of microscopic scarring in the cardiomyopathic heart: Effect of chronic AT(1) suppression. Anal Biochem 316:232–242
18. Sutton SR, Bertsch PM, Newville M, Rivers M, Lanzirotti A, Eng P (2002) Microfluorescence and microtomography analyses of heterogeneous earth and environmental materials. In: Fenter P, Rivers M, Sturchio N, Sutton S (eds) Applications of synchrotron radiation in low-temperature geochemistry and environmental science. Rev Mineral Geochem 49:429–483
19. Chwiej J, Fik-Mazgaj K, Szczerbowska-Boruchowska M, Lankosz M, Ostachowicz J, Adamek D, Simionovici A, Bohic S (2005) Classification of nerve cells from substantia nigra of patients with Parkinson's disease and amyotrophic lateral sclerosis with the use of X-ray fluorescence microscopy and multivariate methods. Anal Chem 77:2895–2900
20. Tomik B, Chwiej J, Szczerbowska-Boruchowska M, Lankosz M, Wojcik S, Adamek D, Falkenberg G, Bohic S, Simionovici A, Stegowski Z, Szczudlik A (2006) Implementation of X-ray fluorescence microscopy for investigation of elemental abnormalities in amyotrophic lateral sclerosis. Neurochem Res 31:321–331
21. Collingwood JF, Mikhaylova A, Davidson M, Batich C, Streit WJ, Terry J, Dobson J (2005) In situ characterization and mapping of iron compounds in Alzheimer's disease tissue. J Alzheimers Dis 7:267–272
22. Geraki K, Farquharson MJ, Bradley DA (2004) X-ray fluorescence and energy dispersive X-ray diffraction for the quantification of elemental concentrations in breast tissue. Phys Med Biol 49:99–110
23. Shimojo N, Homma-Takeda S, Ohuchi K, Shinyashiki M, Sun GF, Kumagai Y (1997) Mercury dynamics in hair of rats exposed to methylmercury by synchrotron radiation X-ray fluorescence imaging. Life Sci 60:2129–2137
24. Minder B, Das-Smaal EA, Brand EF, Orlebeke JF (1994) Exposure to lead and specific attentional problems in school-children. J Learn Disabil 27:393–399
25. Guntern R, Bouras C, Hof PR, Vallet PG (1992) An improved thioflavine S method for staining neurofibrillary tangles and senile plaques in Alzheimer's disease. Experientia 48:8–10
26. Miller LM, Ruppel ME, Ott CH, Lanzirotti A (2005) Development and applications of an epifluorescence module for synchrotron X-ray fluorescence imaging. Rev Sci Instrum 76:066107
27. Lovell MA, Robertson JD, Teesdale WJ, Campbell JL, Markesbery WR (1998) Copper, iron and zinc in Alzheimer's disease senile plaques. J Neurol Sci 158:47–52
28. Szczerbowska-Boruchowska M, Chwiej J, Lankosz M, Adamek D, Wojcik S, Krygowska-Wajs A, Tomik B, Bohic S, Susini J, Simionovici A, Dumas P, Kastyak M (2005) Intraneuronal investigations of organic components and trace elements with the use of synchrotron radiation. X-Ray Spectrometry 34:514–520
29. Bush AI, Pettingell WH, Multhaup G, Paradis M d, Vonsattel JP, Gusella JF, Beyreuther K, Masters CL, Tanzi RE (1994) Rapid induction of Alzheimer A beta amyloid formation by zinc. Science 265:1464–1467
30. Cuajungco MP, Goldstein LE, Nunomura A, Smith MA, Lim JT, Atwood CS, Huang X, Farrag YW, Perry G, Bush AI (2000) Evidence that the beta-amyloid plaques of Alzheimer's disease

represent the redox-silencing and entombment of abeta by zinc. J Biol Chem 275:19439–19442
31. Kalasinsky KS, Magluilo J Jr, Schaefer T (1994) Study of drug distribution in hair by infrared microscopy visualization. J Anal Toxicol 18:337–341
32. Kalasinsky KS (1998) Drug distribution in human hair by infrared microscopy. Cell Mol Biol (Noisy-le-grand) 44:81–87
33. Bantignies JL, Carr GL, Lutz D, Marull S, Williams GP, Fuchs G (2000) Chemical imaging of hair by infrared microspectroscopy using synchrotron radiation. J Cosmet Sci 51:73–90
34. Bertrand L, Doucet J, Dumas P, Simionovici A, Tsoucaris G, Walter P (2003) Microbeam synchrotron imaging of hairs from ancient Egyptian mummies. J Synchrotron Radiat 10:387–392
35. Kempson IM, Skinner WM, Kirkbride KP (2006) Advanced analysis of metal distributions in human hair. Environ Sci Technol 40:3423–3428
36. Blanc D, Zultak M, Rochefort A, Faivre B, Claudet MH, Drobacheff C (1988) Green hair: clinical, chemical and epidemiologic study. Apropos of a case. Ann Dermatol Venereol 115:807–812